Technical Note

Dynamics of Spring Snow Cover Variability over Northeast China

Taotao Zhang [1,2,*] **and Xiaoyi Wang** [3]

1 Key Laboratory of Meteorological Disaster, Ministry of Education (KLME)/International Joint Research Laboratory of Climate and Environment Change (ILCEC)/Collaborative Innovation Center on Forecast and Evaluation of Meteorological Disasters (CIC-FEMD), Nanjing University of Information Science & Technology (NUIST), Nanjing 210044, China
2 School of Atmospheric Sciences, Nanjing University of Information Science & Technology (NUIST), Nanjing 210044, China
3 State Key Laboratory of Tibetan Plateau Earth System and Resources Environment (TPESRE), Institute of Tibetan Plateau Research, Chinese Academy of Sciences, Beijing 100101, China; xiaoyiwang@itpcas.ac.cn
* Correspondence: ttzhang@nuist.edu.cn

Abstract: Spring snow cover variability over Northeast China (NEC) has a profound influence on the local grain yield and even the food security of the country, but its drivers remain unclear. In the present study, we investigated the spatiotemporal features and the underlying mechanisms of spring snow cover variability over NEC during 1983–2018 based on the satellite-derived snow cover data and atmospheric reanalysis products. The empirical orthogonal function (EOF) analysis showed that the first EOF mode (EOF1) explains about 50% of the total variances and characterizes a coherent snow cover variability pattern over NEC. Further analyses suggested that the formation of the EOF1 mode is jointly affected by the atmospheric internal variability and the sea surface temperature (SST) anomaly at the interannual timescale. Specifically, following a negative phase of the atmospheric teleconnection of the Polar–Eurasian pattern, a prominent cyclonic circulation appears over NEC, which increases the snowfall over the east of NEC by enhancing the water vapor transport and decreases the air temperature through reducing the solar radiation and intensifying the cold advection. As a result, the snow cover has increased over NEC. Additionally, the tripole structure of the North Atlantic spring SST anomaly could excite a wave-train-type anomalous circulation propagating to NEC that further regulates the snow cover variability by altering the atmospheric dynamic and thermodynamic conditions and the resultant air temperature and snowfall. Our results have important implications on the understanding of the spring snow cover anomaly over NEC and the formulation of the local agricultural production plan.

Keywords: Northeast China; spring snow cover; interannual variability; Polar–Eurasian pattern; North Atlantic SST

1. Introduction

Northeast China (NEC) is one of the most important commercial grain bases, where the crop yield accounts for more than 20% of the total production of the country, thus playing a crucial role in the local socioeconomic development and even the country's food security [1–3]. Owing to the long cold season over NEC, abundant snow cover accumulates in winter and is preserved into spring, which has notable impacts on local agricultural production. For example, the melting of snow cover during spring provides precious water resources for crop sowing by regulating runoff and soil moisture [4,5]. In addition, by the snow albedo and hydrological effect, spring snow cover can influence the air temperature and precipitation during spring and summer [6–11], which are the key factors affecting seedling emergence, crop growth, and final yield. Therefore, it is critical to advance the understanding of the spring snow cover variability over NEC for the formulation of the local agricultural production plan and the promotion of socioeconomic development.

The snow cover variability over NEC has been a widely considered topic in the recent global warming scenario [12–15]. Numerous studies explored the changes in various snow cover parameters, such as the snow volume, phenology, and duration [16–19]. Some studies found that the snow cover days have significantly increased in recent decades and attributed this to the influence of the mean air temperature [16,17,19], while others suggested that the snow depth has decreased over NEC [18]. These studies have improved our understanding on the responses of snow cover over NEC to the warming climate, but the spatiotemporal features of the snow cover variability on the interannual timescale have not been well documented as yet.

Previous researches suggested that both the atmospheric internal variability and the external forcings play important roles in the snow cover variability over Eurasia and its sub-regions [20–26]. For example, the dominant modes of Eurasian snow cover variations in spring and autumn were found to be influenced by multiple teleconnection patterns, such as the Arctic Oscillation (AO), East Atlantic (EA), Polar–Eurasian pattern (POL), EA-Western Russia (EAWR), West Pacific (WP), and Scandinavia (SCAND) pattern [24–26]. Moreover, North Atlantic Oscillation (NAO) could affect the snow cover variability over Europe during winter through regulating the thermal advection [20–23]. Sun et al. [27] also found that NAO is an important factor shaping the winter snowfall variability over North China. Lu et al. [18] indicated that the snow depth over NEC during spring and autumn is negatively correlated with the intensity of the East Asian Trough and the polar vortex, while the winter snow depth has a close linkage with the Subtropical High intensity.

As for the lower boundary forcings, the sea surface temperature (SST) anomaly over the North Atlantic has been recognized as a crucial driver that can affect the Eurasian snow cover by exciting the eastward propagated wave-train-type anomalous circulations [25,26,28]. The transition of the North Atlantic SST anomaly from a cold phase to a warm phase around the 1990s contributed to the decadal increase in heavy snowfall over NEC [29]. Recently, studies indicated that the Arctic sea ice variabilities also act as a considerable factor responsible for the anomalies of temperature and precipitation over Eurasia, which then could lead to the variations in snow cover [26,30–32]. However, it remains unclear whether there is any influence of the above factors on the spring snow cover variability over NEC.

Therefore, in this study, we aim to, firstly, clarify the characteristics of the interannual variability in the spring snow cover over NEC, and, secondly, unravel the physical mechanism responsible for the snow cover anomalies.

2. Study Area

In the present study, NEC denotes the region of China over 40°–55°N, 115°–135°E, including the Heilongjiang, Jilin, and Liaoning Provinces and the east part of Inner Mongolia (Figure 1). The Inner Mongolia Plateau lies in western NEC, which is mainly covered by grassland and sparse vegetation. Forests are mainly distributed in the Greater and Lesser Khingan Mountains and Changbai Mountain, which stretch from the north to the east and south of NEC. There are wide range of croplands located in the central and east tip of NEC, with flat terrain and low elevation.
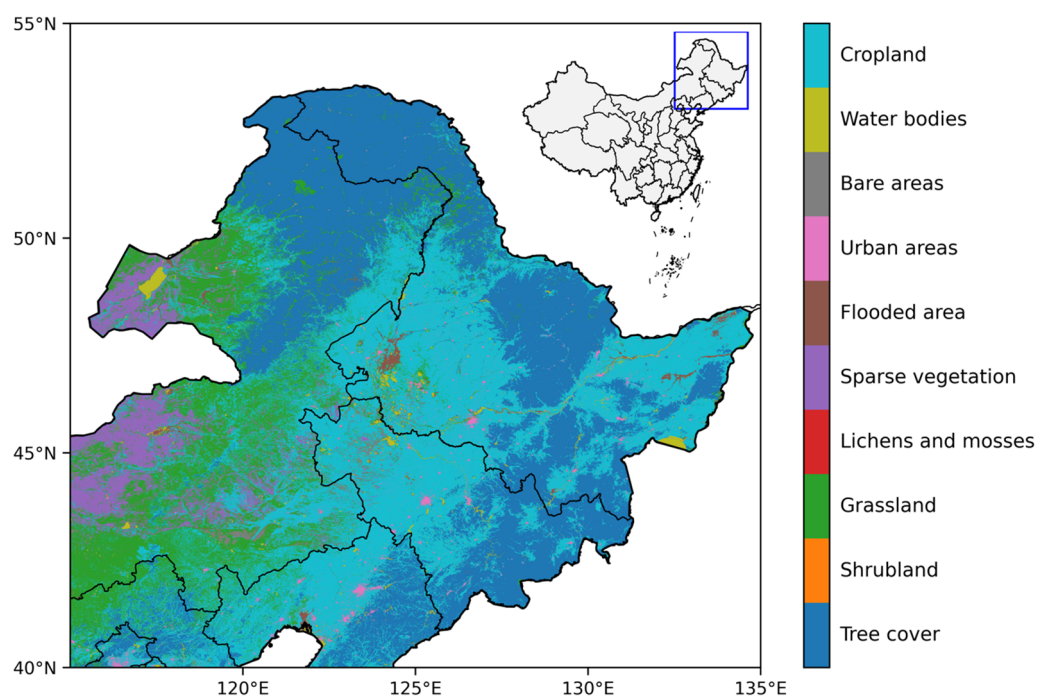
Figure 1. The location and land cover types [33] of Northeast China.

3. Materials and Methods

In the present study, the snow cover fraction (SCF) data were derived from the Northern Hemisphere EASE-Grid 2.0 Weekly Snow Cover and Sea Ice Extent, Version 4, which was provided by the National Snow and Ice Data Center (NSIDC). The NSIDC snow data are available from 1966 to the present with a spatial resolution of $0.25° \times 0.25°$ [34]. We also employed the SCF data from the Japan Aerospace Exploration Agency Satellite Monitoring for Environmental Studies (JASMES) to confirm the reliability of the results from the NSIDC data. The JASMES data are available from 1978 to 2019 with a resolution of 5 km $\times$ 5 km [35]. For ease of analysis, we transformed both the NSIDC and JASMES snow cover data to a monthly $1° \times 1°$ grid based on the linear interpolation.

The monthly surface air temperature (SAT) and precipitation were from the Climate Research Unit, University of East Anglia (CRU TS v4.03). This dataset is available from 1901 to 2020 and has a spatial resolution of $0.5° \times 0.5°$ [36]. The SST data were obtained from the National Oceanic and Atmospheric Administration Extended Reconstructed Sea Surface Temperature (ERSST) v5 dataset. These monthly SST data are on a regular $2° \times 2°$ grid and are available after 1854 [37]. The monthly sea ice concentration data, with a resolution of $1° \times 1°$ and covering 1870 to 2020, are provided by the Hadley Centre Sea Ice and Sea Surface Temperature data set (HadISST1) [38]. The monthly atmospheric variables, including air temperature, horizontal wind, geopotential height, and energy fluxes, were extracted from the National Centers for Environmental Prediction-National Center for Atmospheric Research (NCEP-NCAR) Reanalysis 1 product [39]. The indices of atmospheric teleconnections were downloaded from the National Oceanic and Atmospheric Administration Climate Prediction Center. These datasets have been widely used in previous studies and confirmed to be suitable for climate investigations [34–39].

In order to analyze the variability in SAT, we diagnosed the horizontal thermal advection (T_{adv}), which is calculated according to the following formula [40]:

$$T_{adv} = -u\frac{\partial T}{r\cos\varphi\partial\lambda} - v\frac{\partial T}{r\partial\varphi} \tag{1}$$

where φ and λ represent the latitude and longitude, respectively. u, v, r, and T are the zonal and meridional winds, radius of Earth, and air temperature, respectively.

To detect the propagation of the Rossby wave train, we computed the wave activity flux (WAF) following Takaya and Nakamura [41,42]. The horizontal components of WAF can be written as follows:

$$\text{WAF} = \frac{p\cos\varphi}{2|\mathbf{U}|} \left\{ \begin{array}{l} \frac{U}{\alpha^2\cos^2\varphi}\left[\left(\frac{\partial\psi'}{\partial\lambda}\right)^2 - \psi'\frac{\partial^2\psi'}{\partial\lambda^2}\right] + \frac{V}{\alpha^2\cos\varphi}\left[\frac{\partial\psi'}{\partial\lambda}\frac{\partial\psi'}{\partial\varphi} - \psi'\frac{\partial^2\psi'}{\partial\lambda\partial\varphi}\right] \\ \frac{U}{\alpha^2\cos\varphi}\left[\frac{\partial\psi'}{\partial\lambda}\frac{\partial\psi'}{\partial\varphi} - \psi'\frac{\partial^2\psi'}{\partial\lambda\partial\varphi}\right] + \frac{V}{\alpha^2}\left[\left(\frac{\partial\psi'}{\partial\varphi}\right)^2 - \psi'\frac{\partial^2\psi'}{\partial\varphi^2}\right] \end{array} \right\} \tag{2}$$

where $|\mathbf{U}|$ represents the climatological wind speed; p is the pressure scaled by 1000 hPa; α means the radius of the Earth; φ and λ represent the latitude and longitude; V and U indicate the climatological meridional and zonal wind, respectively; and ψ' denotes the perturbed geostrophic streamfunction.

The Eady growth rate (*EGR*) is employed to quantify the atmospheric baroclinicity [43,44]. The *EGR* can be calculated based on the following equation:

$$EGR = 0.31\frac{|fU_z|}{N} \tag{3}$$

where the f is the Coriolis parameter, U_z denotes the vertical wind shear, and the N is the Brunt–Väisälä frequency. Moreover, the variance in the 2–8-day bandpass-filtered daily geopotential height at 300 hPa is used to indicate the storm track activity.

In light of the lack of part of snow cover data from JASMES and NSIDC in 1981 and 1982, the research period of this paper was set as 1983–2018. The spring snow cover means the average snow cover in March, April, and May. This study aimed to investigate the variations on the interannual timescale; all of the variables needed to be filtered by a 9-year high-pass filter to avoid the potential contamination of the signals of decadal changes and long-term trends. We employed the empirical orthogonal function (EOF) analysis to extract the spatiotemporal features of the spring snow cover variability over NEC. The snow cover anomalies in EOF analysis were weighted by the cosine of the latitudes to account for the reduction in the area toward the higher latitudes [45]. In addition, we calculated the linear correlations of the timeseries of the leading mode of snow cover variability with teleconnections, SST, and sea ice to detect the potential relationships between them. Moreover, the responses of the atmospheric dynamic and thermodynamic conditions to the teleconnections and SST anomalies were examined through linear regression analyses to explore the physical processes responsible for the snow cover variability. The statistical significance was estimated on the basis of the two-tailed Student's *t*-test.

4. Results

4.1. The Leading Mode of Spring Snow Cover Anomaly over NEC

Figure 2 presents the first EOF mode (EOF1) of the interannual variability in NEC spring snow cover during 1983–2018. The EOF1 mode derived from the NSIDC SCF data (Figure 2a) can explain about 50% of the total variances and can be separated from other modes based on the method proposed by North et al. [46]. The spatial pattern of EOF1 characterizes a coherent variation in the spring snow cover over most areas of NEC, with large loading located in the east and north parts of NEC (Figure 2a). The principal component of EOF1 (PC1) shows prominent interannual fluctuation, and the magnitude has experienced an obvious increasing trend since the late 1990s (Figure 2b). This denotes that the interannual variability in the spring snow cover over NEC has strengthened in recent years.
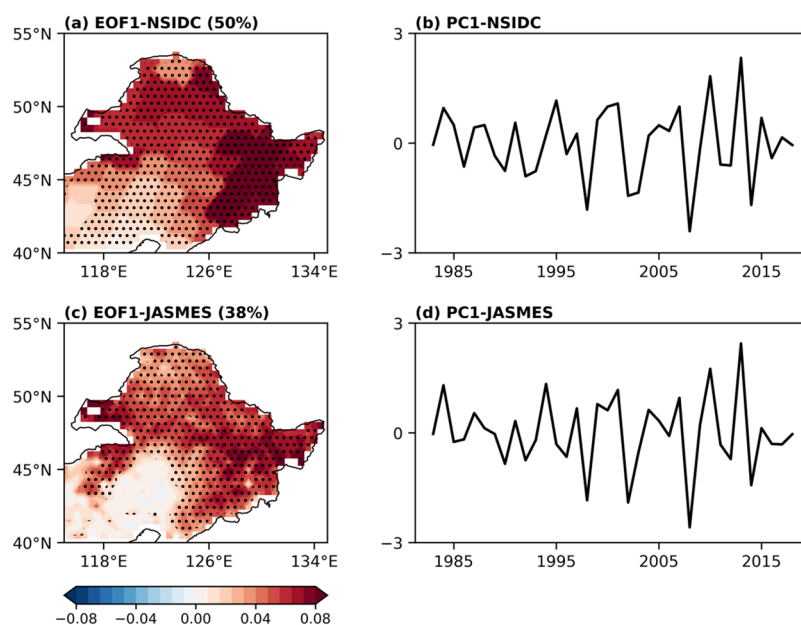
Figure 2. The EOF1 mode of NEC spring snow cover anomaly during 1983–2018. (**a**,**c**) illustrate the spatial patterns of EOF1 mode derived from NSIDC and JASMES snow cover data, respectively. (**b**,**d**) show the corresponding principal component (PC1) of two datasets. The spatial patterns of the EOF1 mode are expressed as the regression of SCF against the respective PC1. The dots represent areas significant at 95% confidence level.

In order to further corroborate the results from the NSIDC data, we also conducted an EOF analysis on the JASMES SCF data. The spatial pattern of the EOF1 mode of the snow cover variability from the JASMES bears a close resemblance to that from the NSIDC, but with a relatively lower variance explanation rate of 38% (Figure 2c). In addition, the correlation coefficient between the PC1 from the JASMES and that from the NSIDC reaches 0.89, exceeding the 99% confidence level (Figure 2d). The consistencies of the EOF results regarding both the spatial pattern and its temporal evolution between two SCF datasets verify the robustness of the features of the EOF1 mode of NEC spring snow cover variability. Although the spatiotemporal features of the snow cover variability from the two datasets are consistent with each other, the EOF1 mode from the NSIDC can explain a larger proportion of the total variances than that from JASMES. Therefore, in the following sections, we mainly use the NSIDC data to investigate the mechanisms of the NEC spring snow cover variability. The main results do not change when the JASMES snow cover data are employed (See Supplementary Material).

4.2. Mechanisms of the Spring Snow Cover Variability over NEC

Variation in snow cover is mainly controlled by the anomalies of snowfall and air temperature, which determine the processes of snow melt and accumulation. In theory, a lower temperature and excessive snowfall in the cold season are conducive to the accumulation of snow cover on the ground, and vice versa [25,26]. Furthermore, the variabilities in snowfall and air temperature are the products of atmospheric circulation anomalies [27,47]. Therefore, the first step is to analyze the EOF1-related simultaneous anomalous atmospheric circulations to identify the potential influencing factors.

Figure 3 exhibits the anomalies of horizontal winds and geopotential height at 200 hPa, 500 hPa, and 850 hPa, which are obtained through regression with the PC1. It is apparent that the anomalous atmospheric circulation patterns at different levels of the troposphere are generally consistent with each other (Figure 3), indicating a quasi-barotropic structure. Specifically, corresponding to the positive phase of PC1, NEC is dominated by a prominent anomalous cyclonic circulation that may contribute to the excessive snow cover over NEC by modulating the precipitation and temperature. From a wider view, there is a clear

meridional dipole pattern of geopotential height anomalies over the north polar region and northeast Asia (Figure 3). This circulation pattern closely resembles that related to the atmospheric teleconnection patterns of AO and POL [48–50], implying that they could act as the potential drivers of the NEC snow cover variability. In addition, a zonal wave-train-type circulation can be seen over the mid–high latitudes that stems from the North Atlantic to NEC (Figure 3), indicating the possible impact of the North Atlantic SST anomaly on the NEC snow cover variation. Therefore, in the following section, we explore the physical mechanisms of the NEC spring snow cover anomaly by mainly considering the contributions of the atmospheric teleconnections and the North Atlantic SST.
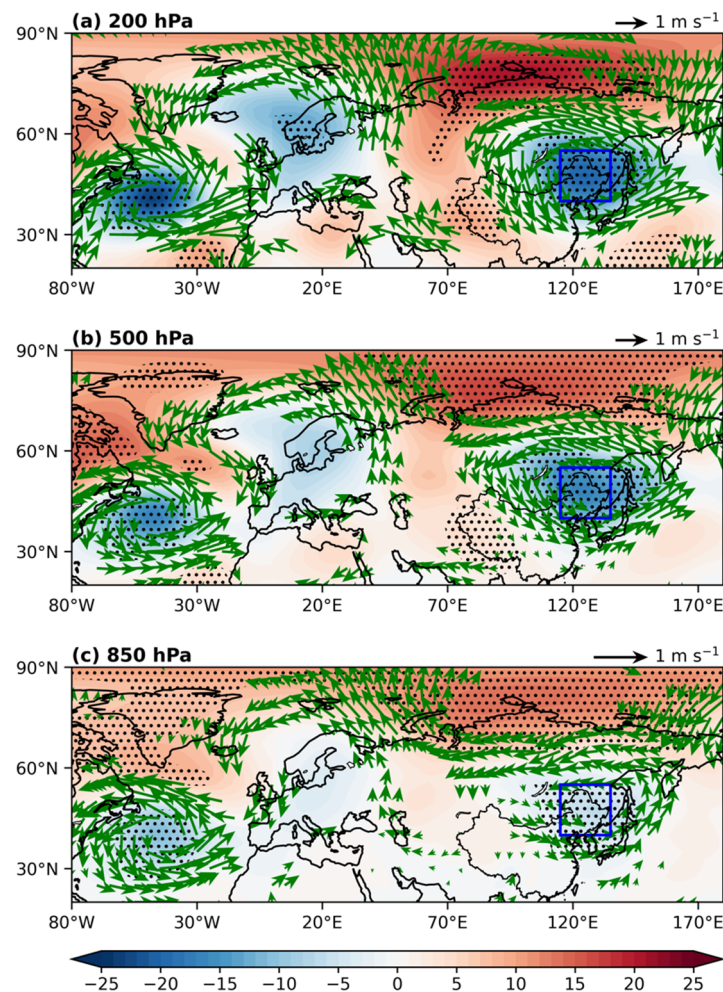

Figure 3. Anomalies of geopotential height (shading; gpm) and wind (vectors; m s^{-1}) at 200 hPa (**a**), 500 hPa (**b**), and 850 hPa (**c**) obtained by regression onto PC1 during 1983–2018. Green vectors and black dots indicate the anomalies of wind and geopotential height reaching the 95% confidence level, respectively. The blue boxes represent the domain of NEC.

4.2.1. Effect of the Polar–Eurasia Pattern

Correlation analyses confirm that the AO and POL have a close connection with the PC1 of the leading mode of NEC snow cover variability, with correlation coefficients of -0.35 ($p < 0.05$) and -0.45 ($p < 0.01$), respectively (Table 1). We also calculated the correlations of PC1 with other major teleconnections that prevailed over Eurasia [48,49], but none of them have a significant correlation with PC1 (Table 1). These results are also robust when the JASMES snow data are used (Table S1). In addition, we note that there is a close connection between AO and POL, with a correlation coefficient of 0.43 ($p < 0.01$). This implies that the linkages of AO and POL with PC1 may not be independent of each other. To check this speculation, we calculated the partial correlations between PC1 and AO (POL)

after removing the effect of POL (AO), respectively. The results show that the correlation between PC1 and POL is still significant after excluding the signal of AO (Figure 4b), suggesting that the influence of POL on the EOF1 mode of NEC snow cover variability is independent of AO. In contrast, the relationship between PC1 and AO substantially weakens when the signal of POL is excluded (Figure 4a). This denotes that the linkage between PC1 and AO may be an artifact of the effect of POL. Therefore, we suggest that the POL is the major factor responsible for the formation of the leading mode of NEC snow cover variation.

Table 1. Correlation coefficients (R) between the PC1 of NEC snow cover variability with the contemporary atmospheric teleconnections. One asterisk and double asterisks indicate the R exceeding the 95% and 99% confidence levels, respectively.

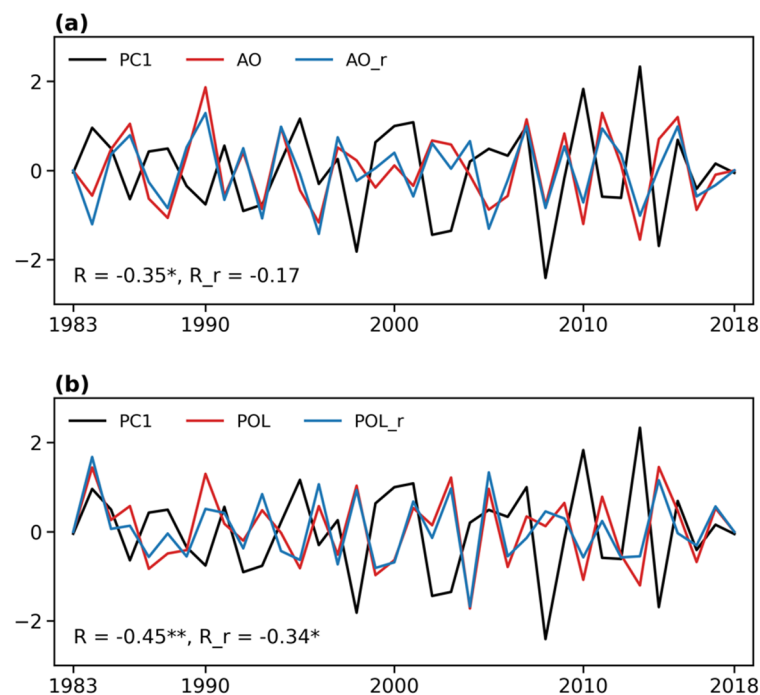| Teleconnection Indices	R
AO	−0.35 *
NAO	−0.11
EA	−0.21
EAWR	−0.04
POL	−0.45 **
SCAND	−0.17
WP	−0.02

Figure 4. (**a**) The correlations of PC1 with the AO (R) and AO_r (R_r). The AO_r represents the residuals of AO where the signal of POL has been linearly removed. (**b**) is the same as (**a**) except for with POL and POL_r. POL_r is the residual of POL where the signal of AO has been linearly removed. The correlation coefficients exceeding the 95% and 99% confidence levels are labeled by one asterisk and double asterisks, respectively.

What are the physical processes involved in the effect of the POL on NEC snow cover anomalies? To answer this question, we explored the POL-related anomalies of geopotential height and horizontal winds. As shown in Figure 5a, in response to the negative phase of POL, the anomalous circulations exhibit a tripole structure at 500 hPa, with two positive anomalies centers of geopotential height over the north high latitudes and northwest Pacific, and one negative anomaly centering around northeast Asia. Accordingly, two anomalous anticyclones and one anomalous cyclone are observed over the corresponding regions

(Figure 5a). The anomalous circulation pattern at the lower troposphere (Figure 5b) closely resembles that at 500 hPa, implying a quasi-barotropic vertical structure of the circulation anomalies related to the POL.
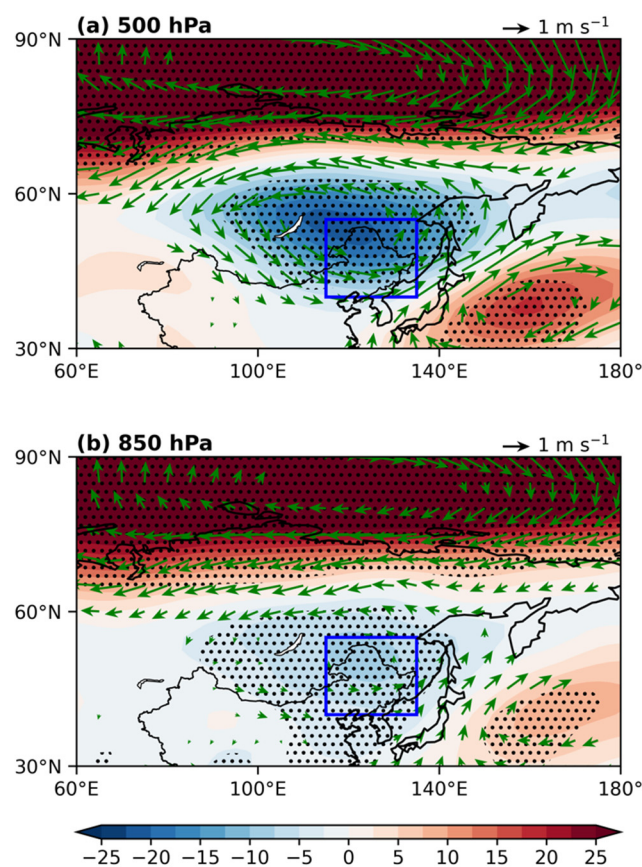

Figure 5. The anomalies of horizontal wind (vectors; m s^{-1}) and geopotential height (shading; gpm) at 500 hPa (**a**) and 850 hPa (**b**) obtained by regression onto the sign-reversed POL index during 1983–2018. The anomalies of wind and geopotential height exceeding the 95% confidence level are labeled by green vectors and black dots, respectively. The blue boxes represent the domain of NEC.

Focusing on northeast Asia, the anomalous southeast flow on the east side of the anomalous cyclone transports the warm and moist air flow northward from the Japan Sea and then converges over the east and north sides of the NEC (Figure 6a), leading to excessive snowfall over the region (Figure 6g). Moreover, the increased cloud cover (Figure 6b) induced by the moisture convergence contributes to the decreased downward shortwave radiation to the north and east boundaries of NEC (Figure 6c), which in turn causes the negative anomalies of SAT there (Figure 6f). As a result, the reduced SAT and the increased snowfall jointly lead to the above normal snow cover over the north and east boundaries of NEC (Figure 6h). In addition, the anomalous northwesterly air flow on the west side of the cyclonic circulation could lead to the invasion of cold and dry air from the higher latitudes to the central part of NEC (Figure 5), which directly results in the negative anomalies of SAT (Figure 6f) through cold advection (Figure 6e). On the other hand, the intrusion of the northwest flow could further indirectly decrease the SAT by reducing the downward longwave radiation (Figure 6d) owing to the lower emissivity of longwave radiation of the dry cold air. Therefore, the positive anomalies of snow cover over central NEC (Figure 6h) may mainly result from the decreased SAT because the snowfall has not changed significantly over the region (Figure 6g). In general, the POL-induced snow cover anomaly pattern is consistent with that related to the EOF1 mode, verifying the crucial role of POL in shaping the spring snow cover variability over NEC.
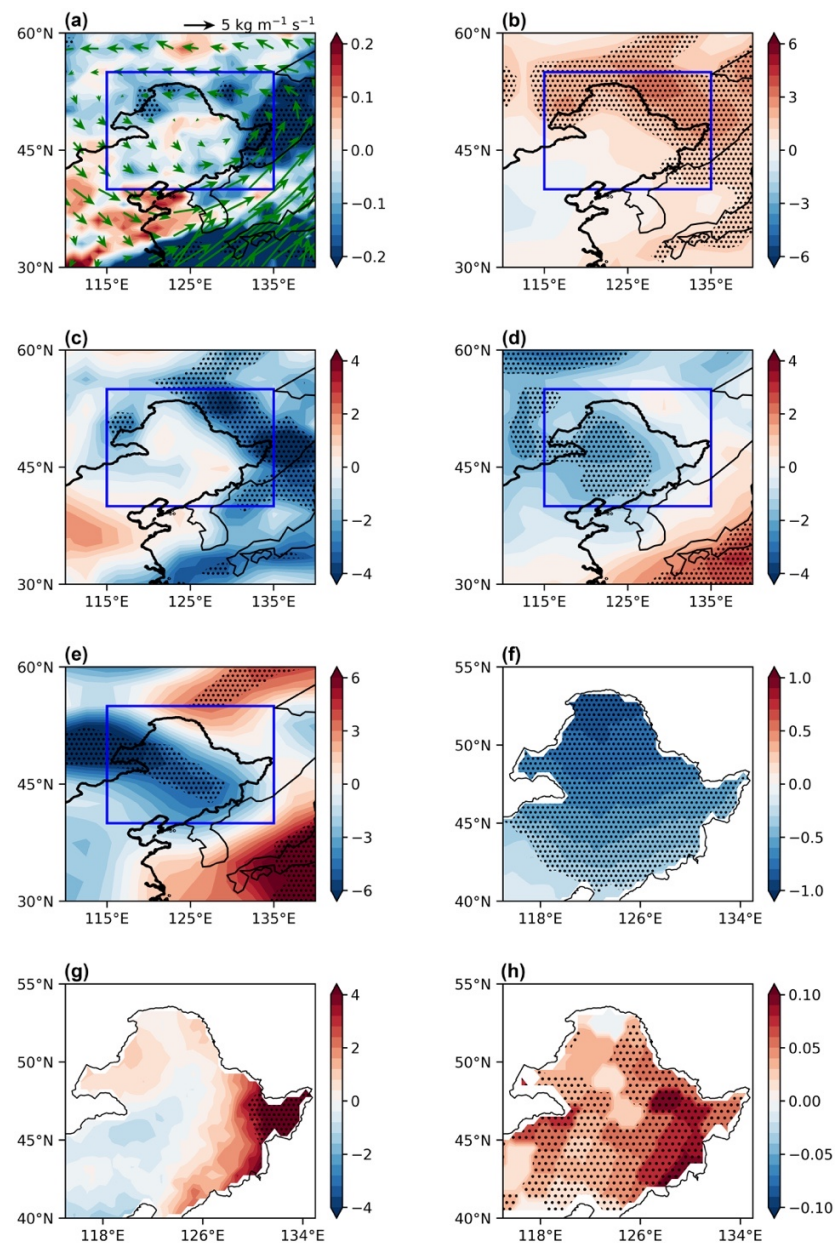
Figure 6. The anomalies of various variables obtained by regression against the sign-reversed POL index. (**a**) Vertical integrated moisture flux (vectors; kg m^{-1} s^{-1}) and its divergence (10^{-5} kg m^{-2} s^{-1}), (**b**) total cloud cover (%), downward shortwave (**c**) and longwave (**d**) radiation flux (W m^{-2}), (**e**) temperature advection (°C month^{-1}), (**f**) SAT (°C), (**g**) snowfall (mm), (**h**) SCF. Black dots imply where the anomalies reach the 95% confidence level. The blue boxes represent the domain of NEC.

4.2.2. Impact of the North Atlantic SST Anomaly

In order to explore the relationship of the North Atlantic SST with the dominant mode of the NEC snow cover anomaly, a regression between the anomalies of the spring SST and PC1 were examined. As illustrated in Figure 7a, the North Atlantic SST anomalies exhibit an apparent tripole pattern, with one negative anomaly centering over the east of North America, and two positive anomalies centering over the subtropics and the south of Greenland, respectively. We further constructed an SST index (SSTI) to quantitatively depict the variability in the tripole SST anomalies. The SSTI is defined as the standardized difference in the area-average SST over the two positive centers and the negative center. There is an intimate connection between PC1 and SSTI, with the correlation coefficient reaching 0.56, exceeding the 99% confidence level (Figure 7b), confirming the potential role

of the North Atlantic tripole SST anomalies in the variability in NEC spring snow cover. Note that these results are supported by the analyses based on the JASMES snow data (Figure S1).
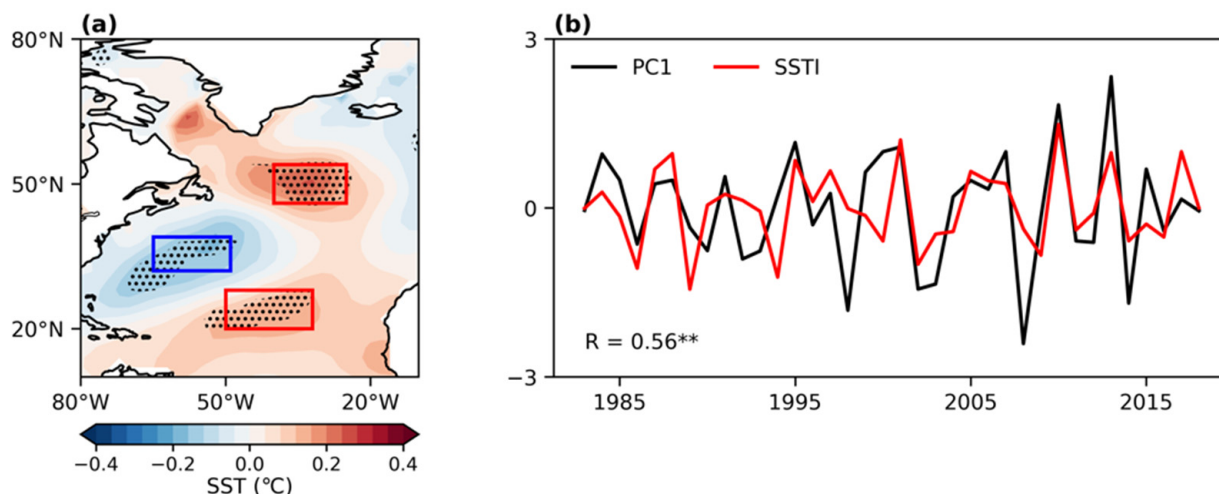

Figure 7. (**a**) SST anomalies over North Atlantic obtained by regression against PC1. (**b**) Timeseries of the SSTI and PC1. Black dots in (**a**) denote the SST anomalies exceeding 95% confidence level. Double asterisks in (**b**) indicate the R exceeding the 99% confidence levels. The regions enclosed by blue and red rectangles are used to compute the SSTI. The domains of three key regions are 46°–54°N, 25°–40°W; 32°–39°N, 49°–65°W; and 20°–28°N, 32°–50°W for the north, central, and south regions, respectively.

Previous studies indicated that the North Atlantic SST anomalies' tripole pattern can regulate climate variations over Eurasia by exciting a wave-train-like anomalous circulation [25,51,52]. Here, we find that following the positive phase of the SSTI, the geopotential height anomalies at 300 hPa exhibit a clear wave train structure (Figure 8a). According to the WAF, we can see that the wave-train-type circulation propagates from the North Atlantic to east Asia, thus acting like a bridge spreading the influence of the North Atlantic SST anomalies on the NEC climate (Figure 8a). How does the tripole SST anomaly excite such a Rossby wave train? Previous studies suggested that the response of the transient eddy activities to the low-level atmospheric baroclinicity is the crucial process responsible for the forcing of the SST anomaly on the atmosphere [53–56]. To unravel this mechanism, we investigated the SSTI-related meridional temperature gradient and the atmospheric baroclinicity at 850 hPa, and anomalies of the storm track at 300 hPa (Figure 8b–d). Following the positive polarity of the SSTI, the temperature gradient has increased over the region between the areas with the negative SST anomalies over the central North Atlantic and the positive SST anomalies over the subtropics (Figure 8b). On the contrary, the decreased temperature gradient is seen over the area between the positive SST anomalies centers over the south of Greenland and the central North Atlantic (Figure 8b). Correspondingly, the strengthened (weakened) atmospheric baroclinicity presents over the regions with an increased (decreased) temperature gradient (Figure 8c). In response to the changes in the atmospheric baroclinicity, reduced and intensified storm tracks are observed over the south of Greenland and the central North Atlantic, respectively (Figure 8d). The enhanced (weakened) transient eddy activity tends to be accompanied by cyclonic (anticyclonic) eddy forcing to its north [57,58]. As a result, the tripole SST anomalies could lead to the positive and negative geopotential height anomalies over southern Greenland and central North Atlantic, respectively, which further excite the wave train propagating to east Asia (Figure 8a).
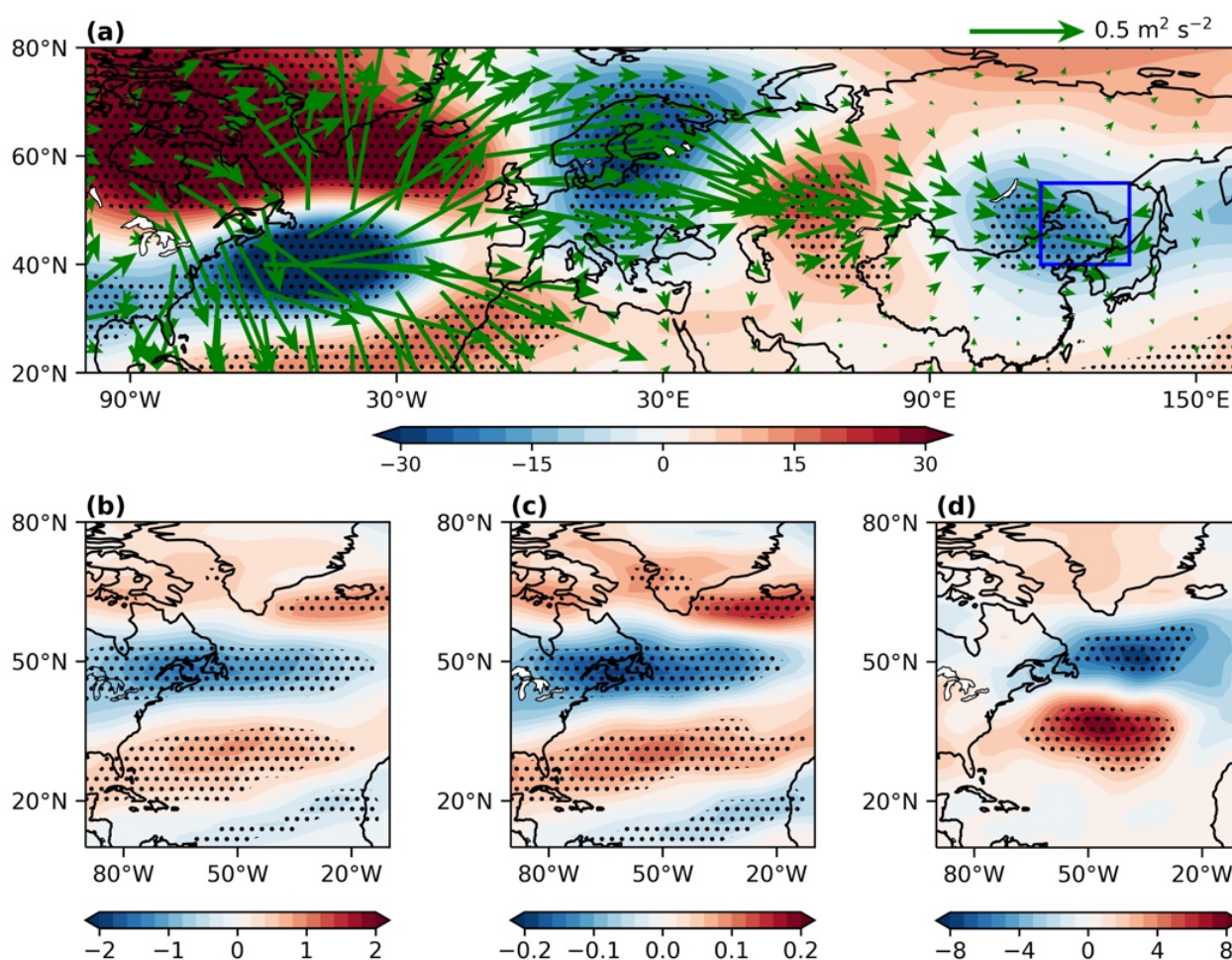
Figure 8. Anomalies of (**a**) geopotential height (shading; gpm) and the related WAF (vectors) at 300 hPa, (**b**) meridional air temperature gradient (10^{-6} K m^{-1}) and (**c**) Eady growth rate (day^{-1}) at 850 hPa, (**d**) storm track at 300 hPa (gpm) obtained by regression onto SSTI. Stippling indicates the 95% confidence level. The blue box represents the domain of NEC.

The wave train type circulation has significantly negative height anomalies centering around the NEC (Figures 8a and 9a). Controlled by this cyclonic circulation, the south and southeast winds on the east side of the cyclonic circulation bring abundant water vapor northward (Figure 9b) and lead to above-normal snowfall over the south NEC (Figure 9g). In addition, the convergence of the water vapor results in the positive anomalies of cloud cover over the north NEC (Figure 9c), which would further reduce the incoming solar radiation and hence the decreased SAT over there (Figure 9d,f). On the west side of the cyclone, the northwesterly air flow causes the decreased SAT over the south NEC through cold advection (Figure 9e,f). The SSTI-related snow cover variability over NEC shows a coherent positive anomalies pattern, with two prominent anomalies centering over the south and north parts of NEC, respectively (Figure 9h). According to our above analyses, the snowfall has no significant change over north NEC (Figure 9g), which would exert limited influence on the snow cover anomaly over the region. Therefore, the increased snow cover in the north center mainly results from the decreased SAT, while that in the south center could be attributed to the combined effect of the reduced SAT and increased snowfall (Figure 9f–h).
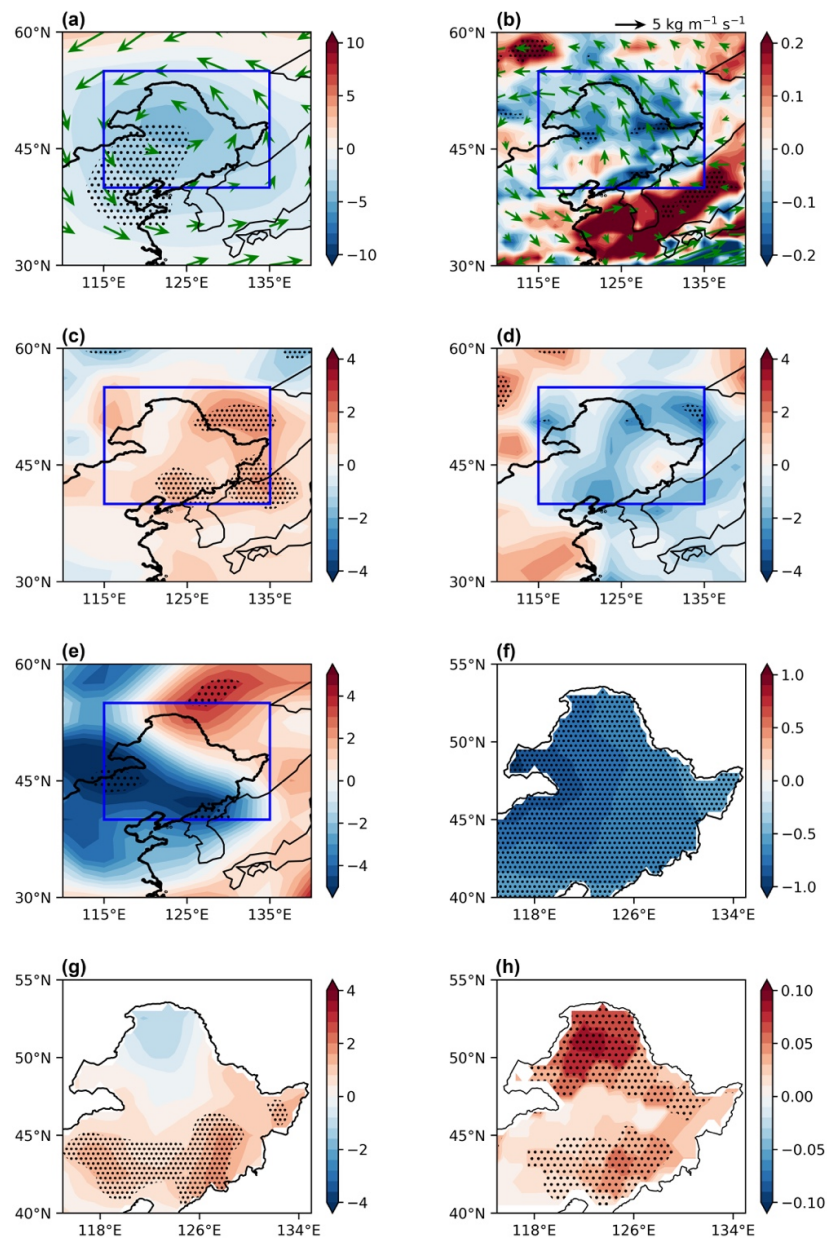
Figure 9. The anomalies of various variables obtained by regression against the SSTI. (**a**) Geopotential height and wind at 850 hPa, (**b**) vertical integrated moisture flux (vectors; kg m^{-1} s^{-1}) and its divergence (10^{-5} kg m^{-2} s^{-1}), (**c**) total cloud cover (%), (**d**) downward shortwave radiation flux (W m^{-2}), (**e**) temperature advection (°C month^{-1}), (**f**) SAT (°C), (**g**) snowfall (mm), and (**h**) SCF. Dotted areas indicate where the anomalies are significant at the 95% confidence level. The blue boxes represent the domain of NEC.

5. Conclusions and Discussion

This study successfully achieved both of its objectives by (1) clarifying the characteristics of the interannual variability in NEC spring snow cover (1983–2018) and (2) identifying the physical mechanisms responsible for the main drivers creating the variability in NEC spring snow cover. This was accomplished by analyzing satellite-derived snow cover data along with the analysis of the effects of atmospheric patterns and SST. The EOF analysis was used to obtain the leading mode of the NEC snow cover anomaly. The EOF1 mode can explain about half of the total variances and features a coherent snow cover variability over NEC. Further analyses found that the atmospheric teleconnection pattern of POL and the tripole SST anomalies over the North Atlantic play a major role in the formation of the

EOF1 mode. Specifically, the POL-related anomalous circulations transport moisture to the east and north sides of NEC, resulting in excessive snowfall over the region. In addition, the circulation-induced cold advection and reduced solar radiation lead to the negative anomalies of SAT dominating the whole NEC. The decreased air temperature and increased snowfall contribute to the excessive snow cover over NEC. The North Atlantic tripole SST anomalies can shape the NEC spring snow cover variability by exciting a wave-train-type anomalous circulation that propagates from the North Atlantic to NEC. Controlled by the SST-induced anomalous cyclone, the snowfall has increased over the south part of NEC, while the SAT over the whole NEC has significantly decreased. These anomalies of SAT and snowfall are conducive to the accumulation of snow cover. Our results can substantially improve the understanding of the variability in spring snow cover over NEC and provide scientific support for making local agricultural policies.

We note that although the POL and the tripole SST anomalies have profound impacts on the dominant mode of the spring snow cover variability over NEC, they can jointly account for about 50% of the variances. This implies that there should be other influencing factors responsible for the NEC snow cover variability. Previous studies suggested that the Arctic sea ice variation can exert important influence on the NEC climate variability [27,59]. Here, we additionally examined the possible relationship between Arctic sea ice and NEC snow cover. As exhibited in Figure 10 (also in Figure S2), the correlations between PC1 and the spring sea ice are generally weak, suggesting the limited contribution of the Arctic sea ice variation on the NEC spring snow cover variations. Therefore, in future studies, we should investigate other potential drivers to further improve the understanding of the mechanisms of the snow cover variability over NEC. Previous studies found that the connections between some influencing factors and regional climate anomalies have weakened [60–62] or strengthened [10,63,64] in recent years. It remains unknown if the influences of the POL and the tripole SST anomalies on the NEC snow cover variability would change in a future warming climate. In addition, this study only concentrates on the interannual variability; the characters and the underlying physical mechanisms of the decadal change and the long-term trend of the NEC snow cover have not been well documented as yet. These issues should be explored in the following studies using longer observational data and model simulation. Moreover, the extraction of snow cover data from satellite images can be influenced by vegetation [65]. It is necessary to strengthen snow monitoring over vegetation-covered areas, which is beneficial to improve the accuracy of snow cover data.
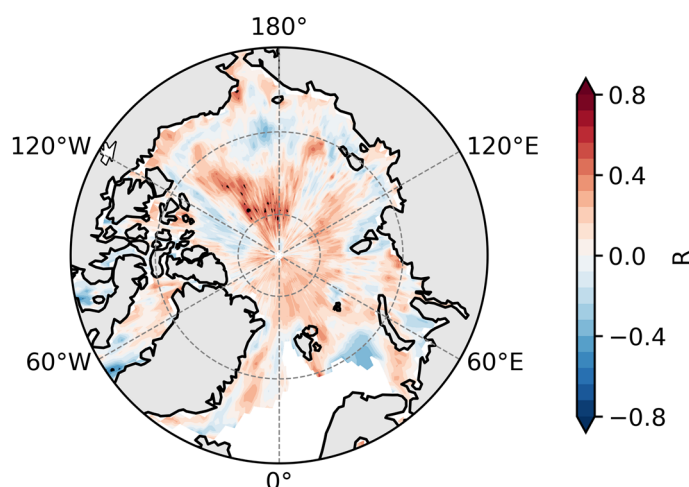

Figure 10. Correlations between PC1 of NEC spring snow cover variability and simultaneous sea ice variations. Dots denote the correlations exceeding the 95% confidence level.

References

1. Yang, J.; Chen, Y.; Wang, Q. Cultivated Land Resources and Grain Production Potential in the Three Northeast Provinces. *Chin. J. Soil Sci.* **2017**, *48*, 1055–1060. (In Chinese)
2. Han, D.; Zhao, J.; Hu, Q. Study on the change characteristics of food crop yield in Northeast China and its response to meteorological drought. *J. China Agricul. Uni.* **2021**, *26*, 188–200. (In Chinese)
3. Zhen, Z.; Chen, S.; Yin, T.; Gastellu-Etchegorry, J.-P. Improving Crop Mapping by Using Bidirectional Reflectance Distribution Function (BRDF) Signatures with Google Earth Engine. *Remote Sens.* **2023**, *15*, 2761. [CrossRef]
4. Qi, W.; Feng, L.; Liu, J.; Yang, H. Snow as an important natural reservoir for runoff and soil moisture in Northeast China. *J. Geophys. Res. Atmos.* **2020**, *125*, e2020JD033086. [CrossRef]
5. Li, Y.; Liu, D.; Li, T.; Fu, Q.; Liu, D.; Hou, R.; Meng, F.; Li, M.; Li, Q. Responses of spring soil moisture of different land use type to snow cover in Northeast China under climate change background. *J. Hydrol.* **2022**, *608*, 127610. [CrossRef]
6. Barnett, T.P.; Dumenil, L.; Schlese, U.; Roeckner, E.; Latif, M. The effect of Eurasian snow cover on regional and global climate variations. *J. Atmos. Sci.* **1989**, *46*, 661–685. [CrossRef]
7. Cohen, J.; Rind, D. The Effect of Snow Cover on the Climate. *J. Clim.* **1991**, *4*, 689–706. [CrossRef]
8. Wu, R.; Zhao, P.; Liu, G. Change in the contribution of spring snow cover and remote oceans to summer air temperature anomaly over Northeast China around 1990. *J. Geophys. Res. Atmos.* **2014**, *119*, 663–676. [CrossRef]
9. Halder, S.; Dirmeyer, P.A. Relation of Eurasian snow cover and Indian summer monsoon rainfall: Importance of the delayed hydrological effect. *J. Clim.* **2017**, *30*, 1273–1289. [CrossRef]
10. Zhang, T.; Wang, T.; Feng, Y.; Li, X.; Krinner, G. An emerging impact of Eurasian spring snow cover on summer rainfall in Eastern China. *Env. Res. Lett.* **2021**, *16*, 054012. [CrossRef]
11. Sun, Y.; Chen, H.; Zhu, S.; Zhang, J.; Wei, J. Influence of the Eurasian spring snowmelt on summer land surface warming over Northeast Asia and its associated mechanism. *J. Clim.* **2021**, *34*, 4851–4869. [CrossRef]
12. Chen, S.; Yang, Q.; Xie, H.; Zhang, H.; Lu, P.; Zhou, C. Spatiotemporal variations of snow cover in northeast China based on flexible multiday combinations of moderate resolution imaging spectroradiometer snow cover products. *J. Appl. Remote Sens.* **2014**, *8*, 084685. [CrossRef]
13. Ma, N.; Yu, K.; Zhang, Y.; Zhai, J.; Zhang, Y.; Zhang, H. Ground observed climatology and trend in snow cover phenology across China with consideration of snow-free breaks. *Clim. Dyn.* **2020**, *55*, 2867–2887. [CrossRef]
14. Wang, Y.; Zheng, Z. Spatial Representativeness Analysis for Snow Depth Measurements of Meteorological Stations in Northeast China. *J. Hydrometeorol.* **2020**, *21*, 791–805. [CrossRef]
15. Zou, Y.; Sun, P.; Ma, Z.; Lv, Y.; Zhang, Q. Snow Cover in the Three Stable Snow Cover Areas of China and Spatio-Temporal Patterns of the Future. *Remote Sens.* **2022**, *14*, 3098. [CrossRef]

16. Zhang, X.; Zang, S.; Sun, L. Spatial-temporal variation characteristics of snow cover days in Northeast China in the past 40 years and their relationship with climatic factors. *Adv. Earth Sci.* **2018**, *33*, 958–968. (In Chinese)

17. Zhou, X.; Zhao, C.; Li, N. Spatiotemporal Variation of Snow and its Response to Climate Change in Northeast China. *Plateau Meteor.* **2021**, *40*, 875–886. (In Chinese)

18. Lu, Q.; Li, B.; Wang, Z. The relationship between spatial and temporal change of snow cover depth and atmospheric circulation in Northeast China from 1979 to 2014. *J. Glaciol. Geocryol.* **2018**, *40*, 907–915. (In Chinese)

19. Guo, H.; Wang, X.; Guo, Z.; Chen, S. Assessing Snow Phenology and Its Environmental Driving Factors in Northeast China. *Remote Sens.* **2022**, *14*, 262. [CrossRef]

20. Henderson, G.R.; Leathers, D.J. European snow cover extent variability and associations with atmospheric forcings. *Int. J. Climatol.* **2010**, *30*, 1440–1451. [CrossRef]

21. Seager, R.; Kushnir, Y.; Nakamura, J.; Ting, M.; Naik, N. Northern Hemisphere winter snow anomalies: ENSO, NAO and the winter of 2009/10. *Geophys. Res. Lett.* **2010**, *37*, L14703. [CrossRef]

22. Kim, Y.; Kim, K.-Y.; Kim, B.-M. Physical mechanisms of European winter snow cover variability and its relationship to the NAO. *Clim. Dyn.* **2013**, *40*, 1657–1669. [CrossRef]

23. Wegmann, M.; Rohrer, M.; Santolaria-Otín, M.; Lohmann, G. Eurasian autumn snow link to winter North Atlantic Oscillation is strongest for Arctic warming periods. *Earth Syst. Dynam.* **2020**, *11*, 509–524. [CrossRef]

24. Gastineau, G.; García-Serrano, J.; Frankignoul, C. The influence of autumnal Eurasian snow cover on climate and its link with Arctic sea ice cover. *J. Clim.* **2017**, *30*, 7599–7619. [CrossRef]

25. Zhang, T.; Wang, T.; Zhao, Y.; Xu, C.; Feng, Y.; Liu, D. Drivers of Eurasian Spring Snow-Cover Variability. *J. Clim.* **2021**, *34*, 2037–2052. [CrossRef]

26. Zhang, T.; Feng, Y.; Chen, H. Revealing the formation of the dipole mode of Eurasian snow cover variability during late autumn. *J. Geophys. Res. Atmos.* **2023**, *128*, e2022JD038233. [CrossRef]

27. Sun, B.; Wang, H.J.; Wu, B.W.; Xu, M.; Zhou, B.T.; Li, H.X.; Wang, T. Dynamic Control of the Dominant Modes of Interannual Variability of Snowfall Frequency in China. *J. Clim.* **2021**, *34*, 2777–2790. [CrossRef]

28. Sun, C.; Zhang, R.; Li, W.; Zhu, J.; Yang, S. Possible impact of North Atlantic warming on the decadal change in the dominant modes of winter Eurasian snow water equivalent during 1979–2015. *Clim. Dyn.* **2019**, *53*, 5203–5213. [CrossRef]

29. Zhou, B.T.; Wang, Z.Y.; Sun, B.; Hao, X. Decadal Change of Heavy Snowfall over Northern China in the Mid-1990s and Associated Background Circulations. *J. Clim.* **2021**, *34*, 825–837. [CrossRef]

30. Bailey, H.; Hubbard, A.; Klein, E.S.; Mustonen, K.R.; Akers, P.D.; Marttila, H.; Welker, J.M. Arctic sea-ice loss fuels extreme European snowfall. *Nat. Geosci.* **2021**, *14*, 283–288. [CrossRef]

31. Xu, B.; Chen, H.; Gao, C.; Zhou, B.; Sun, S.; Zhu, S. Regional response of winter snow cover over the Northern Eurasia to late autumn Arctic sea ice and associated mechanism. *Atmos. Res.* **2019**, *222*, 100–113. [CrossRef]

32. Santolaria-Otín, M.; García-Serrano, J.; Ménégoz, M.; Bech, J. On the observed connection between Arctic sea ice and Eurasian snow in relation to the winter North Atlantic Oscillation. *Env. Res. Lett.* **2020**, *15*, 124010. [CrossRef]

33. ESA. Land Cover CCI Product User Guide Version 2. Tech. Rep. 2017. Available online: https://maps.elie.ucl.ac.be/CCI/viewer/download/ESACCI-LC-Ph2-PUGv2_2.0.pdf (accessed on 30 October 2023).

34. Brodzik, M.J.; Armstrong, R. *Northern Hemisphere EASE-Grid 2.0 weekly snow cover and sea ice extent, version 4*; NASA National Snow and Ice Data Center Distributed Active Archive Center. 2013. Available online: https://doi.org/10.5067/P7O0HGJLYUQU (accessed on 10 November 2022).

35. Hori, M.; Sugiura, K.; Kobayashi, K.; Aoki, T.; Tanikawa, T.; Kuchiki, K.; Niwano, M.; Enomoto, H. A 38-year (1978–2015) Northern Hemisphere daily snow cover extent product derived using consistent objective criteria from satellite-borne optical sensors. *Remote Sens. Env.* **2017**, *191*, 402–418. [CrossRef]

36. Harris, I.; Osborn, T.J.; Jones, P.; Lister, D. Version 4 of the CRU TS monthly high-resolution gridded multivariate climate dataset. *Sci. Data* **2020**, *7*, 109. [CrossRef]

37. Huang, B.; Thome, P.W.; Banzon, V.F.; Boyer, T.; Cherupin, G.; Lawrimore, J.H.; Menne, M.J.; Smith, T.M.; Vose, R.S.; Zhang, H.-M. Extended Reconstructed Sea Surface Temperature, version 5 (ERSSTv5): Upgrades, validation and intercomparisons. *J. Clim.* **2017**, *30*, 8179–8205. [CrossRef]

38. Rayner, N.A.; Parker, D.E.; Horton, E.B.; Folland, C.K.; Alexander, L.V.; Rowell, D.P.; Kent, E.C.; Kaplan, A. Global analyses of sea surface temperature, sea ice, and night marine air temperature since the late nineteenth century. *J. Geophys. Res. Atmos.* **2003**, *108*, 4407. [CrossRef]

39. Kalnay, E.; Kanamitsu, M.; Kistler, R.; Collins, W.; Deaven, D.; Gandin, L.; Iredell, M.; Saha, S.; White, G.; Woollen, J.; et al. The NCEP/NCAR 40-Year Reanalysis Project. *Bull. Amer. Meteorol. Soc.* **1996**, *77*, 437–472. [CrossRef]

40. Holton, J.R. *An introduction to Dynamic Meteorology*; Academic Press: London, UK, 1992.

41. Takaya, K.; Nakamura, H. A formulation of a wave-activity flux for stationary Rossby waves on a zonally varying basic flow. *Geophys. Res. Lett.* **1997**, *24*, 2985–2988. [CrossRef]

42. Takaya, K.; Nakamura, H. A formulation of a phase-independent wave-activity flux for stationary and migratory quasigeostrophic eddies on a zonally varying basic flow. *J. Atmos. Sci.* **2001**, *58*, 608–627. [CrossRef]

43. Eady, E.T. Long waves and cyclone waves. *Tellus* **1949**, *1*, 33–52. [CrossRef]

44. Lindzen, R.S.; Farrell, B. A simple approximate result for the maximum growth rate of baroclinic instabilities. *J. Atmos. Sci.* **1980**, *37*, 1648–1654. [CrossRef]

45. North, G.R.; Moeng, F.J.; Bell, T.L.; Cahalan, R.F. The latitude dependence of the variance of zonally averaged quantities. *Mon. Wea. Rev.* **1982**, *110*, 319–326. [CrossRef]

46. North, G.R.; Bell, T.L.; Cahalan, R.F.; Moeng, F.J. Sampling Errors in the Estimation of Empirical Orthogonal Functions. *Mon. Weather Rev.* **1982**, *110*, 699–706. [CrossRef]

47. Chen, S.F.; Wu, R.; Liu, Y. Dominant modes of interannual variability in Eurasian surface air temperature during boreal spring. *J. Clim.* **2016**, *29*, 1109–1125. [CrossRef]

48. Wallace, J.M.; Gutzler, D.S. Teleconnections in the geopotential height field during the Northern Hemisphere winter. *Mon. Weather Rev.* **1981**, *109*, 784–812. [CrossRef]

49. Barnston, A.G.; Livezey, R.E. Classification, seasonality and persistence of low-frequency atmospheric circulation patterns. *Mon. Wea. Rev.* **1987**, *115*, 1083–1126. [CrossRef]

50. Thompson, D.W.J.; Wallace, J.M. The Arctic oscillation signature in the wintertime geopotential height and temperature fields. *Geophys. Res. Lett.* **1998**, *25*, 1297–1300. [CrossRef]

51. Han, Z.; Luo, F.; Wan, J. The observational influence of the North Atlantic SST tripole on the early spring atmospheric circulation. *Geophys. Res. Lett.* **2016**, *43*, 2998–3003. [CrossRef]

52. Song, Y.; Chen, H. Influence of the Late-Winter North Atlantic Tripole Sea Surface Temperature Anomalies on Spring Land Surface Temperature in Mid-to-High Latitudes of Western Eurasia. *J. Clim.* **2023**, *36*, 4933–4950. [CrossRef]

53. Peng, S.; Mysak, L.A.; Ritchie, H.; Derome, J.; Dugas, B. The differences between early and midwinter atmospheric responses to sea surface temperature anomalies in the Northwest Atlantic. *J. Clim.* **1995**, *8*, 137–157. [CrossRef]

54. Kushnir, Y.; Robinson, W.A.; Bladé, I.; Hall, N.M.J.; Peng, S.; Sutton, R. Atmospheric GCM response to extratropical SST anomalies: Synthesis and evaluation. *J. Clim.* **2002**, *15*, 2233–2256. [CrossRef]

55. Nie, Y.; Zhang, Y.; Chen, G.; Yang, X. Delineating the barotropic and baroclinic mechanisms in the midlatitude eddy-driven jet response to lower-tropospheric thermal forcing. *J. Atmos. Sci.* **2016**, *73*, 429–448. [CrossRef]

56. Chen, S.F.; Wu, R.; Chen, W.; Hu, K.M.; Yu, B. Structure and dynamics of a springtime atmospheric wave train over the North Atlantic and Eurasia. *Clim. Dyn.* **2020**, *54*, 5111–5126. [CrossRef]

57. Lau, N.C. Variability of the Observed Midlatitude Storm Tracks in Relation to Low-Frequency Changes in the Circulation Pattern. *J. Atmos. Sci.* **1988**, *45*, 2718–2743. [CrossRef]

58. Cai, M.; Yang, S.; Dool, H.; Kousky, V. Dynamical implications of the orientation of atmospheric eddies: A local energetics perspective. *Tellus Dyn. Meteorol. Oceanogr.* **2007**, *59*, 127–140. [CrossRef]

59. Gao, K.; Tang, Y.; Chen, D. Influence of Arctic Sea ice and Interdecadal Pacific Oscillation on the recent increase of winter extreme snowfall in Northeast China. *Atmos. Res.* **2023**, *295*, 107030. [CrossRef]

60. Wu, R.; Liu, G.; Ping, Z. Contrasting Eurasian spring and summer climate anomalies associated with western and eastern Eurasian spring snow cover changes. *J. Geophys. Res. Atmos.* **2014**, *119*, 7410–7424. [CrossRef]

61. Wang, Z.; Wu, R.; Duan, A.-M.; Qu, X. Influence of eastern Tibetan Plateau spring snow cover on North American air temperature and its interdecadal change. *J. Clim.* **2020**, *33*, 5123–5139. [CrossRef]

62. Zhang, T.; Wang, T.; Krinner, G.; Wang, X.; Gasser, T.; Peng, S.; Piao, S.; Yao, T. The Weakening Relationship between Eurasian Spring Snow Cover and Indian Summer Monsoon Rainfall. *Sci. Adv.* **2019**, *5*, eaau8932. [CrossRef]

63. Han, T.; Tang, G.; Zhou, B.; Hao, X.; Li, S. Strengthened relationship between sea ice in East Siberian Sea and midsummer rainfall in Northeast China. *Clim. Dyn.* **2023**, *60*, 3749–3763. [CrossRef]

64. Chen, S.; Wu, R. Interdecadal changes in the relationship between interannual variations of spring North Atlantic SST and Eurasian surface air temperature. *J. Clim.* **2017**, *30*, 3771–3787. [CrossRef]

65. Zhen, Z.; Chen, S.; Yin, T.; Gastellu-Etchegorry, J.-P. Globally quantitative analysis of the impact of atmosphere and spectral response function on 2-band enhanced vegetation index (EVI2) over Sentinel-2 and Landsat-8. *ISPRS J. Photogramm. Remote Sens.* **2023**, *205*, 206–226. [CrossRef]